IEEE Access
Multidisciplinary | Rapid Review | Open Access Journal

Received 3 December 2024, accepted 20 February 2025, date of publication 27 February 2025, date of current version 7 March 2025.

Digital Object Identifier 10.1109/ACCESS.2025.3546435

THEORY

Delay-Controlled Frequency Tuning of a MEMS Sensor for Neuromorphic Acoustic Sensing

HERMANN FOLKE JOHANN ROLF[1], PETRO FEKETA[2], AND THOMAS MEURER[1], (Senior Member, IEEE)

[1]Digital Process Engineering Group, Institute of Mechanical Process Engineering and Mechanics, Karlsruhe Institute of Technology, 76131 Karlsruhe, Germany
[2]School of Mathematics and Statistics, Victoria University of Wellington, Wellington 6140, New Zealand

Corresponding author: Hermann Folke Johann Rolf (folke.rolf@kit.edu)

This work was supported by the Deutsche Forschungsgemeinschaft (DFG)—German Research Foundation under Project 434434223–SFB 1461.

ABSTRACT Frequency tunability marks the ability to change the characteristic frequency of an oscillator. For MEMS sensors, this is usually achieved by exploiting a sophisticated geometry with a nonlinear stress-strain relationship. This is known as active frequency tuning. However, MEMS sensors with such geometries are difficult to manufacture and the characteristic frequency can have a lower limit, which is constrained by the material constants and geometry of the MEMS sensor. To address this issue, we propose a different approach to enable active frequency tunability, which is based on designing a feedback loop with a controllable time delay. We show by analyzing the necessary condition of the Hopf theorem that the characteristic frequency of this system can be increased indefinitely or decreased to 90% of its original value by appropriately adjusting the delay and the feedback strengths. These observations can be explained by combining with the undelayed and delayed feedback loop, which implies that the phase and the amplitude of the feedback signal can be controlled. In addition, the gain of the sensor becomes tunable, since the Andronov-Hopf bifurcation can be controlled with this feedback loop. These results are particularly interesting for mimicking the cochlea functionality, as the cochlear is assumed to exhibit an Andronov-Hopf bifurcation. Hence, this approach can be, e.g., used for neuromorphic acoustic sensing, while keeping the geometry of this MEMS sensor as simple as possible.

INDEX TERMS Andronov-Hopf Bifurcation, delayed feedback, envelope model, frequency tunability, gain tunability, microelectronic-mechanical system (MEMS), MEMS sensor, neuromorphic acoustic sensing, neuromorphic engineering.

I. INTRODUCTION

An oscillator, whose characteristic frequency can be changed, is called frequency tunable. For a microelectronic-mechanical system (MEMS) sensor, the characteristic frequency is usually determined once the geometry (or the material composition) is fixed and adjusting this frequency can be enabled by employing either passive or active methods. In the former methods the geometry or the material composition of the system is adjusted [1], [2]. In the latter methods the characteristic frequency is continuously tuned with a controllable input. For this, the actuator typically exploits electrothermal [3], [4], [5] or electrostatic effects [6], [7], [8], [9], [10], which change the deflection of the mechanical system, so that strain becomes a function of (small) actuation amplitudes [3], [4], [5], [9], [10]. Due to this geometric nonlinearity, the characteristic frequency can be either decreased or increased by assigning the actuator accordingly [3], [4].

A MEMS sensor with a tunable characteristic frequency has multiple advantages. On the one hand, this system is robust against inaccurate manufacturing processes, material defects, and aging, since the desired characteristic frequency can be achieved by tuning the MEMS sensor actively [3].

The associate editor coordinating the review of this manuscript and approving it for publication was Mark Kok Yew Ng.

© 2025 The Authors. This work is licensed under a Creative Commons Attribution 4.0 License.
For more information, see https://creativecommons.org/licenses/by/4.0/

On the other hand, a frequency tunable MEMS sensor is sensitive to a wider frequency range while preserving its bandwidth.

In this paper, a thermally actuated cantilevered MEMS sensor based on [11], [12], [13], [14], [15] is considered. By choosing the feedback signal correctly, this MEMS sensor exhibits an Andronov-Hopf bifurcation [15], [16], [17], [18]. In particular, this bifurcation can be used to model the remarkable dynamics of the cochlea [19], [20], [21] as it implies frequency selectivity and compression, i.e., small amplitudes are amplified and large amplitudes are attenuated [19], [20], [22], [23], [24], [25]. However, when exploiting this bifurcation for neuromorphic acoustic sensing, many MEMS sensors are needed to cover a broad frequency interval, so that frequency tunability is important for the design of neuromorphic acoustic sensors. In addition, by introducing such a feedback loop in MEMS sensors with geometric nonlinearities, the measurement is frequency modulated [4], [5] and the system can become chaotic [5], [26]. This is a tremendous disadvantage for sensing purposes as the input signal cannot be reconstructed in both cases.

In contrast, the Andronov-Hopf bifurcation is classically used to show that a (stable) limit cycle can emerge in an oscillator. This comes from the fact that an oscillator, which exhibits an Andronov-Hopf bifurcation, has two different regimes. The oscillator can change between these regimes by adjusting the bifurcation parameter. If the oscillator is in the sub-critical regime, the oscillator will be (locally) asymptotically stable, i.e., the oscillator will converge to its equilibrium. If the oscillator is in the super-critical regime, a (stable) limit cycle will emerge. In addition, the point separating these regimes is called critical point [27]. For instance, this idea has been used to analyze systems in biology [28], [29], [30], [31], engineering [32], and physics [33], [34], [35].

We want to enable frequency tunability of a thermally actuated cantilevered MEMS sensor by extending the proportional feedback in [13], [14], and [15] with a delayed feedback loop. For this, the feedback loop consists of the sum of an feedforward signal, the undelayed measurement, and the delayed measurement, so that the system has four controllable parameters, i.e., the feedforward signal, the time delay, and the feedback strengths of the undelayed and delayed measurement. The concept of this setup is visualized in Figure 1 and this idea is based on the frequent observation that a time delay can change the characteristic frequency of a system, see, e.g., [36], [37], [38], and [39]. The tunability analysis is done by investigating the emergence of Andronov-Hopf bifurcations. If this system is frequency tunable at the critical point, the same property then follows directly for a neighborhood around this point [39].

It turns out that four Andronov-Hopf bifurcations emerge and that characteristic frequency can be tuned close to their critical critical point. In particular, the increase of the characteristic frequency is indefinite, while the decrease allows a reduction down to 90% of the natural frequency of the MEMS sensor. Additionally, it is shown that the gain of the MEMS sensor can be controlled by adjusting the distance to the critical point.

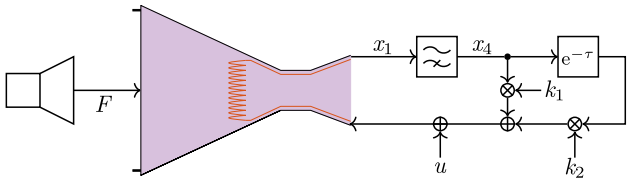

FIGURE 1. Setup for the thermally actuated, cantilevered MEMS sensor with a undelayed and delayed feedback.

The remainder of the paper is structured as follows: The preliminaries for this paper are discussed in Section II. This includes the introduction of the mathematical model of the cantilevered MEMS sensor and the summary of the bifurcation analysis of the MEMS sensor with undelayed feedback. In Section III, the frequency tunability of the MEMS sensor with delayed and undelayed feedback is investigated by analyzing emergence of Andronov-Hopf bifurcations in terms of delay and the characteristic frequency at the critical point. These results are then evaluated numerically in Section IV by determining the characteristic frequency at the critical point as a function of the controllable parameters. Some remarks conclude this paper.

II. MEMS SENSORS

Subsequently, the preliminary results on the dynamics of the MEMS sensor and the its frequency tunability is discussed. This MEMS sensor consists of a three-layered cantilever with a silicon layer as a fundament, a silicon oxide layer for isolation, and an aluminum layer for electrothermal actuation. Moreover, the deflection of this sensor can be measured by a piezoelectric strain gauge, which is placed at the clamped end of the sensor [11], [12], [13], [14], [15]. The model of the MEMS sensor is obtained by considering the dominant mode. This model describes the evolution of the temperature, deflection and velocity and is derived by employing modal reduction on the equations of thermo-elasticity, see [5] and [12]. A high pass filter is used to estimate the velocity and thus to remove the offset of the equilibrium of deflection with the transfer function $g(s) = \kappa Ts/(1+Ts)$ for $\kappa, T > 0$. The setup is visualized in Figure 1. In addition, it is assumed that the output of the high pass filter is fed into the heater of the MEMS sensor by an undelayed and delayed feedback. For this, let $\bullet_\tau(t) = \bullet(t-\tau)$ with a positive (and controllable) delay $\tau \geq 0$. The resulting model reads

$$\dot{\boldsymbol{x}} = \boldsymbol{f}(\boldsymbol{x}, \boldsymbol{x}_\tau, F, u), \quad t > 0, \tag{1a}$$

$$\boldsymbol{x}(\vartheta) = \boldsymbol{x}_0(\vartheta), \quad \vartheta \in [-\tau, 0], \tag{1b}$$

$$y = x_4, \quad t \geq 0 \tag{1c}$$

with

$$\boldsymbol{f}(\boldsymbol{x}, \boldsymbol{x}_\tau, F, u) = \begin{bmatrix} 1 \\ -\omega_0^2 x_1 - \dfrac{\omega_0}{Q_0} x_2 + \alpha x_3 + \dfrac{1}{\rho h} F \\ -\beta x_3 + \zeta (k_1 x_4 + k_2 x_{4,\tau} + u)^2 \\ -\dfrac{1}{T} x_4 + \kappa x_2 \end{bmatrix}, \quad \text{(1d)}$$

the state vector $\boldsymbol{x}(t) = [x_1(t), x_2(t), x_3(t), x_4(t)] \in \mathbb{R}^4$, the (uncontrollable) external stimuli $F(t) \in \mathbb{R}$, the (controllable) voltage $u(t) \in \mathbb{R}$, and the output $y(t) \in \mathbb{R}$. The state vector is composed of the deflection x_1, the velocity x_2, the ambient temperature x_3, and the estimated velocity x_4. Additional parameters are given by the natural frequency $\omega_0 > 0$, the Q-factor $Q_0 > 0$, the transfer factors $\alpha > 0$, $\zeta = \gamma / R^2 > 0$, $\gamma > 0$, the density $\rho > 0$, the height $h > 0$ of the MEMS sensor, the time constant $\beta > 0$, the resistance $R > 0$, the feedback strengths $k_1 \in \mathbb{R}$, and $k_2 \in \mathbb{R}$ and the initial conditions $\boldsymbol{x}_0(\vartheta) \in \mathbb{R}^4$. In this paper, we will show that the feedback strengths k_1 and k_2 and the delay τ can be used to mimic the cochlear dynamics and enable frequency tunability.

A. LINEARIZATION

To address the bifurcation analysis of (1), the system has to be linearized around an equilibrium $\boldsymbol{x}_{\text{eq}} \in \mathbb{R}^4$, where the equilibria of (1) are determined by asserting $\dot{\boldsymbol{x}}_{\text{eq}} = \boldsymbol{0}$, $\boldsymbol{x}_{\tau,\text{eq}} = \boldsymbol{x}_{\text{eq}}$, $F = 0$ and $u_{\text{eq}} = u_{\text{DC}} \in \mathbb{R}$. These assumptions imply $\boldsymbol{f}(\boldsymbol{x}_{\text{eq}}, \boldsymbol{x}_{\text{eq}}, 0, u_{\text{DC}}) = \boldsymbol{0}$, which results in an unique equilibrium

$$\boldsymbol{x}_{\text{eq}} = \begin{bmatrix} \dfrac{\alpha u_{\text{DC}}^2}{\beta \omega_0^2} & 0 & \dfrac{u_{\text{DC}}^2}{\beta} & 0 \end{bmatrix}^{\text{T}}.$$

The linearization of (1) is then determined by

$$\Delta \dot{\boldsymbol{x}} = A_0 \Delta \boldsymbol{x} + A_1 \Delta \boldsymbol{x}_\tau + B \Delta \boldsymbol{v} \quad \text{(2a)}$$

with $\Delta \boldsymbol{x} = \boldsymbol{x} - \boldsymbol{x}_{\text{eq}}$ and $\Delta \boldsymbol{v} = [F, u - u_{\text{DC}}]^{\text{T}}$. Herein, the system and input matrices are given by

$$A_0 = \partial_{\boldsymbol{x}} \boldsymbol{f} = \begin{bmatrix} 0 & 1 & 0 & 0 \\ -\omega_0^2 & -\dfrac{\omega_0}{Q_0} & \alpha & 0 \\ 0 & 0 & -\beta & 2 u_{\text{DC}} \zeta k_1 \\ 0 & \kappa & 0 & -\dfrac{1}{T} \end{bmatrix}, \quad \text{(3a)}$$

$$A_1 = \partial_{\boldsymbol{x}_\tau} \boldsymbol{f} = \begin{bmatrix} 0 & 0 & 0 & 0 \\ 0 & 0 & 0 & 0 \\ 0 & 0 & 0 & 2 u_{\text{DC}} \zeta k_2 \\ 0 & 0 & 0 & 0 \end{bmatrix}, \quad \text{(3b)}$$

$$B = \begin{bmatrix} \partial_F \boldsymbol{f} \\ \partial_u \boldsymbol{f} \end{bmatrix} = \begin{bmatrix} 0 & \dfrac{1}{\rho h} & 0 & 0 \\ 0 & 0 & \zeta & 0 \end{bmatrix}^{\text{T}}. \quad \text{(3c)}$$

The emergence of the Andronov-Hopf bifurcations is investigated by analyzing the characteristic function

$$g_{\text{CF}}(\lambda) = \det(A_0 + A_1 \text{e}^{-\tau\lambda} - \lambda I_4) \quad \text{(4)}$$

with the identity matrix $I_4 \in \mathbb{R}^{4\times4}$ and the variable $\lambda \in \mathbb{C}$ [40], [41], [42]. Inserting (3a) and (3b) in (4) results in

$$g_{\text{CF}}(\lambda) = \lambda^4 + a_3 \lambda^3 + a_2 \lambda^2 + \left[a_1 - b_1 \left(k_1 + k_2 e^{-\tau\lambda} \right) \right] \lambda + a_0 \quad \text{(5)}$$

with the parameters

$$\begin{aligned} a_3 &= \frac{1}{T} + \frac{\omega_0}{Q_0} + \beta, \\ a_2 &= \omega_0^2 + \frac{\beta}{\tau} + \frac{\beta\omega_0}{Q_0} + \frac{\omega_0}{Q_0 T}, \\ a_1 &= \beta\omega_0^2 + \frac{\omega_0^2}{T} + \frac{\beta\omega_0}{Q_0 T}, \\ a_0 &= \frac{\beta\omega_0^2}{T}, \\ b_1 &= 2\alpha\zeta\kappa u_{\text{DC}}. \end{aligned}$$

B. PROBLEM STATEMENT

The emergence of Andronov-Hopf bifurcations in system (1) was analyzed in [16] in the delay-free case, i.e., $k_2 = 0$ and $\tau = 0$. For this, the feedback strength k_1 is chosen as the bifurcation parameter. In this case the system (1) undergoes two Andronov-Hopf bifurcations, where the critical points and the frequencies at these points are given by

$$k_{\text{H}}^{\pm}\big|_{\tau=0} = \frac{2a_1 - a_2 a_3 \pm a_3 \sqrt{a_2^2 - 4a_0}}{2b_1}, \quad \text{(6a)}$$

$$\omega_{\text{H}}^{\pm}\big|_{\tau=0} = \sqrt{\frac{a_2 \pm \sqrt{a_2^2 - 4a_0}}{2}}. \quad \text{(6b)}$$

However, this approach has a significant drawback, since the characteristic frequency of this system has a strict lower limit. This limit is caused by the geometry and the material constants of the cantilevered MEMS structure, and it can be approximated by the lowest mode of the MEMS sensors. In general, the modes of a beam are given by

$$\omega_i = \frac{\lambda_i^2}{l^2} \sqrt{\frac{EI}{\rho S}}$$

with the length $l > 0$, the Young modulus $E > 0$, the inertia $I > 0$, the density ρ, the cross-section surface $S > 0$, and a constant $\lambda_i > 0$ [43, Example 6.7]. For a cantilever, the constant λ_i satisfies

$$\cos(\lambda_i)\cosh(\lambda_i) = 0$$

for all $i \in \mathbb{N}$. Hence, lower frequencies in this setup cannot be achieved without increasing the length l and cross-section surface S of the MEMS structure or changing the materials. However, both approaches are limited by physical constraints. In scope of this work, the effects of a controllable time delay τ on the emergence of the Andronov-Hopf bifurcations and the characteristic frequency of (1) are analyzed. Based on [39], this approach is promising, since

the characteristic frequency can be increased or decreased by assigning the time delay τ and the feedback strengths k_1 and k_2. Frequency tunability will be analyzed subsequently both analytically and numerically as the characteristic equation (5) has infinitely many solutions. In the analytic investigation, the emergence of Andronov-Hopf bifurcations is evaluated. With this, an analytic relationship between the characteristic frequency at the critical points and the controllable parameter k_1, k_2, u_{DC} and τ is derived and the frequency tunability can be analyzed. In the numerical investigation, the characteristic frequency is evaluated in the complete sub-critical and super-critical regime by computing the imaginary part of dominant eigenvalue of (5). In general, this transcendental equation cannot be solved analytically.

III. ANALYTICAL RESULTS

The bifurcation analysis of (1) is based on the Hopf Theorem in $\mathbb{R}^n$, see, e.g., [26] and [27]. Hence, this analysis is split into two steps: First, the critical point is determined by deriving conditions, such that (5) has two complex conjugated eigenvalues on the imaginary axis. Second, the crossing condition is evaluated by showing that the sensitivity, i.e., the real part of the derivative of the complex conjugated eigenvalues on the imaginary axis in terms of the bifurcation parameter, is not vanishing. It has to be stressed that the sign of the sensitivity can be used to deduce whether the bifurcation is super-critical or sub-critical. If the sensitivity is positive, the bifurcation is super-critical, while the bifurcation is sub-critical, if the sensitivity is negative. In contrast to the local properties, the non-local properties, i.e., the stability of the emerging limit cycle, is not evaluated. There are two reasons for this: First, the super-critical regime is not desirable for sensor applications, since the oscillator should react only to external inputs F. Otherwise the external input F would be mixed with the limit cycle of the oscillator, so that the inputs are distorted. Second, it has been discussed in [16] that the dominant mode model of the MEMS sensor with the undelayed feedback has an unstable limit cycle. This implies that system (1) has also an unstable limit cycle and thus (1) is unstable in the super-critical regime.

A. NECESSARY CONDITION OF THE HOPF THEOREM

Subsequently, the necessary conditions for an Andronov-Hopf bifurcation are analyzed. For this, the bifurcation parameter is assumed to be the time delay τ. The critical point can be derived by inserting $\lambda = \mathrm{i}\omega_{\mathrm{H}}$ and $\tau = \tau_{\mathrm{H}}$ into (5) with the characteristic frequency $\omega_{\mathrm{H}} > 0$ and the critical delay $\tau_{\mathrm{H}} > 0$. This yields

$$\begin{aligned} 0 = {} & \omega_{\mathrm{H}}^4 - \mathrm{i}a_3\omega_{\mathrm{H}}^3 - a_2\omega_{\mathrm{H}}^2 \\ & + \mathrm{i}\left[a_1 - b_1\left(k_1 + k_2 e^{-\mathrm{i}\tau_{\mathrm{H}}\omega_{\mathrm{H}}}\right)\right]\omega_{\mathrm{H}} + a_0. \end{aligned} \tag{7}$$

It has to be noted that the result will not change, if $\lambda = -\mathrm{i}\omega_{\mathrm{H}}$ is inserted, since (5) has real-valued coefficients. Eq. (7) can be solved by dividing it into real and imaginary part, which results in

$$0 = \omega_{\mathrm{H}}^4 - a_2\omega_{\mathrm{H}}^2 - k_2 b_1 \sin(\tau_{\mathrm{H}}\omega_{\mathrm{H}})\omega_{\mathrm{H}} + a_0, \tag{8a}$$

$$0 = -a_3\omega_{\mathrm{H}}^3 + \left[a_1 - b_1\left(k_1 + k_2\cos(\tau_{\mathrm{H}}\omega_{\mathrm{H}})\right)\right]\omega_{\mathrm{H}}. \tag{8b}$$

Solving (8a) for $\sin(\tau_{\mathrm{H}}\omega_{\mathrm{H}})$, yields

$$\sin(\tau_{\mathrm{H}}\omega_{\mathrm{H}}) = \frac{\omega_{\mathrm{H}}^4 - a_2\omega_{\mathrm{H}}^2 + a_0}{k_2 b_1 \omega_{\mathrm{H}}}. \tag{9}$$

Eq. (9) only admits real-valued solution for the critical delay τ_{H}, if $\left|\frac{\omega_{\mathrm{H}}^4 - a_2\omega_{\mathrm{H}}^2 + a_0}{k_2 b_1 \omega_{\mathrm{H}}}\right| \leq 1$. Inserting (9) into (8b) and noting that $\sin^2(\tau_{\mathrm{H}}\omega_{\mathrm{H}}) + \cos^2(\tau_{\mathrm{H}}\omega_{\mathrm{H}}) = 1$, results in

$$\begin{aligned} 0 = {} & (a_1 - k_1 b_1)\,\omega_{\mathrm{H}} - a_3\omega_{\mathrm{H}}^3 \\ & - \operatorname{sign}(k_2 b_1)\sqrt{k_2^2 b_1^2 \omega_{\mathrm{H}}^2 + \left(\omega_{\mathrm{H}}^4 - a_2\omega_{\mathrm{H}}^2 + a_0\right)^2}. \end{aligned} \tag{10}$$

By adding the square root term, taking the square of the result and sorting the terms, (10) is transformed into

$$\begin{aligned} 0 = {} & a_0^2 - \left[2a_0a_2 - (a_1 - b_1k_1)^2 + b_1^2k_2^2\right]\omega_{\mathrm{H}}^2 \\ & + \left[a_2^2 + 2a_0 - 2a_3\,(a_1 - b_1k_1)\right]\omega_{\mathrm{H}}^4 \\ & + \left(a_3^2 - 2a_2\right)\omega_{\mathrm{H}}^6 + \omega_{\mathrm{H}}^8. \end{aligned} \tag{11}$$

In particular, (11) and (8) have the same zeros with respect to ω_{H}, if

$$\begin{aligned} & \left[k_2 b_1 > 0 \ \wedge \ (a_1 - k_1 b_1) - a_3\omega_{\mathrm{H}}^2 > 0\right] \\ & \qquad \vee \ \left[k_2 b_1 < 0 \ \wedge \ (a_1 - k_1 b_1) - a_3\omega_{\mathrm{H}}^2 < 0\right], \end{aligned} \tag{12}$$

since the square root term in (10) has to be positive. After substituting $\omega_{\mathrm{H}}^2 = z$, a quartic polynomial with respect to z arises, which is given by

$$\begin{aligned} 0 = {} & a_0^2 - \left[2a_0a_2 - (a_1 - b_1k_1)^2 + b_1^2k_2^2\right]z \\ & + \left[a_2^2 + 2a_0 - 2a_3\,(a_1 - b_1k_1)\right]z^2 \\ & + \left(a_3^2 - 2a_2\right)z^3 + z^4, \end{aligned} \tag{13}$$

so that (11) can be solved analytically. Note that the numerical analysis of these results is discussed in Section IV.

B. SUFFICIENT CONDITION OF THE HOPF THEOREM

The sufficient condition of the Hopf Theorem is satisfied, if the sensitivity of the real-part of the eigenvalues, which cross the imaginary axis, with respect to the bifurcation parameter τ is not vanishing. This condition can be expressed by

$$d = \operatorname{num}\left(\operatorname{Re}\left(\frac{\mathrm{d}\lambda}{\mathrm{d}\tau}\bigg|_{\lambda=\mathrm{i}\omega_{\mathrm{H}}}\right)\right) \neq 0 \tag{14}$$

with the operator $\operatorname{num}(n(z)/d(z)) = n(z)$, which takes the numerator of a irreducible rational function $n(z)/d(z)$. In addition, the direction of movement of the eigenvalues is determined by the sign of d. If $\operatorname{sign}(d) = 1$, the eigenvalues

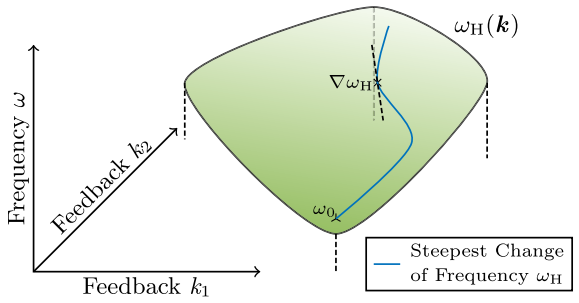

FIGURE 2. Sketch of the steepest change of the characteristic frequency.

cross from left half complex plane to right half complex plane. While, the eigenvalues cross from right to left half complex plane, if $\text{sign}(d) = -1$.

With these considerations, the sensitivity of the eigenvalues with respect to the bifurcation parameter τ can be determined by taking the derivative of (5) with respect to τ and solving the resulting equation for $\frac{\mathrm{d}\lambda}{\mathrm{d}\tau}$. This yields

$$\frac{\mathrm{d}\lambda}{\mathrm{d}\tau} = -\frac{b_1 k_2 \lambda^2}{\mathrm{e}^{\tau\lambda}} \left(\frac{\mathrm{d}g_{\mathrm{CF}}}{\mathrm{d}\tau}\right)^{-1}. \tag{15}$$

with

$$\frac{\mathrm{d}g_{\mathrm{CF}}}{\mathrm{d}\tau} = \left[\lambda\left(3a_3\lambda + 2a_2 + 4\lambda^2\right) + a_1 - b_1k_1\right] + b_1k_2(\tau\lambda - 1).$$

Inserting (15) into (14) after simplification, results in

$$d = -b_1k_2\omega_{\mathrm{H}}^2\left[\left(b_1k_1 - a_1 + 3a_3\omega_{\mathrm{H}}^2\right)\cos\left(\tau_{\mathrm{H}}\omega_{\mathrm{H}}\right) + \left(2a_2\omega_{\mathrm{H}} - 4\omega_{\mathrm{H}}^3\right)\sin\left(\tau_{\mathrm{H}}\omega_{\mathrm{H}}\right) + b_1k_2\right]. \tag{16}$$

The further analysis of (16) is rather involved. This can be seen by exploiting $\sin^2(\tau_{\mathrm{H}}\omega_{\mathrm{H}}) + \cos^2(\tau_{\mathrm{H}}\omega_{\mathrm{H}}) = 1$, and inserting (9) into (16), so that

$$d = -\omega_{\mathrm{H}}\left[2\left(a_2 - 2\omega_{\mathrm{H}}^2\right)\left(\omega_{\mathrm{H}}^4 - a_2\omega_{\mathrm{H}}^2 + a_0\right)\omega_{\mathrm{H}} + b_1^2k_2^2\omega_{\mathrm{H}} - \left(a_1 - b_1k_1 - 3a_3\omega_{\mathrm{H}}^2\right) \times\sqrt{b_1^2k_2^2\omega_{\mathrm{H}}^2 - \left(\omega_{\mathrm{H}}^4 - a_2\omega_{\mathrm{H}}^2 + a_0\right)^2}\right] \tag{17}$$

arises. By asserting $d = 0$, this equation can be transformed again into a quartic polynomial. Hence, the analysis of the sufficient condition is also done numerically.

C. STEEPEST CHANGE OF THE CHARACTERISTIC FREQUENCY

The controllable time delay influences the characteristic frequency in a nonlinear fashion, i.e. the characteristic frequency can be seen as a function of the feedback strengths k_1 and k_2, so that $\omega_{\mathrm{H}} = \omega_{\mathrm{H}}(k_1, k_2)$. To showcase the effects of the controllable time delay on the characteristic frequency we are looking for a specific relation between the feedback strengths leading to the steepest change of the characteristic frequency. A sketch of this approach is given in Figure 2. To enable a more stable computation, the normalized gradient is used, so that the feedback $\boldsymbol{k}_{\mathrm{o}} = [k_{1,\mathrm{o}}, k_{2,\mathrm{o}}]^{\mathrm{T}}$ is determined by

$$\boldsymbol{k}_{\mathrm{o}}[j+1] = \boldsymbol{k}_{\mathrm{o}}[j] + (-1)^l \frac{\epsilon\nabla\omega_{\mathrm{H}}(\boldsymbol{k}_{\mathrm{o}}[j])}{\|\nabla\omega_{\mathrm{H}}(\boldsymbol{k}_{\mathrm{o}}[j])\|}, \quad \boldsymbol{k}_{\mathrm{o}}[0] = \boldsymbol{k}_0$$

with the gradient $\nabla\omega_{\mathrm{H}}(\boldsymbol{k_o}[j]) \in \mathbb{R}^2$, the step size $\epsilon > 0$, and the initial conditions $\boldsymbol{k}_0 \in \mathbb{R}$ for all $l = 1, 2$. Note that the direction of the steepest change is determined by l. The direction of the feedback $\boldsymbol{k}_{\mathrm{o}}$ will follow the steepest decent, if $l = 1$. In contrast, if $l = 2$, the direction of the feedback $\boldsymbol{k}_{\mathrm{o}}$ will follow the steepest ascend. The gradient is given by

$$\nabla\omega_{\mathrm{H}} = \begin{bmatrix} -\frac{b_1\omega_{\mathrm{H}}}{C}\sqrt{b_1^2k_2^2\omega_{\mathrm{H}}^2 - \left(\omega_{\mathrm{H}}^4 - a_2\omega_{\mathrm{H}}^2 + a_0\right)^2} \\ -\text{sign}(b_1k_2)\frac{b_1^2k_2\omega_{\mathrm{H}}^2}{C} \end{bmatrix}$$

with

$$C = 2\left(a_2 - 2\omega_{\mathrm{H}}^2\right)\left(\omega_{\mathrm{H}}^4 - a_2\omega_{\mathrm{H}}^2 + a_0\right)\omega_{\mathrm{H}} + b_1^2k_2^2\omega_{\mathrm{H}} + \left[b_1k_1 + 3a_3\omega_{\mathrm{H}}^2 - a_1\right] \times\sqrt{b_1^2k_2^2\omega_{\mathrm{H}}^2 - \left(\omega_{\mathrm{H}}^4 - a_2\omega_{\mathrm{H}}^2 + a_0\right)^2}.$$

In addition, the conditions (12) and $|k_1 + k_2| < |k_{\mathrm{H}}^{\pm}|$ can be asserted, so that the system (1) is in the sub-critical regime. The numerical results on the steepest change and the implications of this assumption are further discussed in Section IV.

D. SYSTEM RESPONSE AND TUNABILITY

Finally, the reaction of system (1) to a harmonic excitation with respect to F is evaluated to demonstrate its frequency tunability. This is done by determining the equilibrium of the so-called envelope model [44], [45], [46]. In particular, the envelope model is derived by employing the time-dependent Fourier series

$$\boldsymbol{x}_{\tilde{\tau}} = \boldsymbol{q}_{0,\tilde{\tau}} + \sum_{j=1}^{n}\left[\boldsymbol{q}_{2j-1,\tilde{\tau}}\cos(j\omega_{\mathrm{ex}}(t-\tilde{\tau})) + \boldsymbol{q}_{2j,\tilde{\tau}}\sin(j\omega_{\mathrm{ex}}(t-\tilde{\tau}))\right], \tag{18a}$$

$$F = w_0 + \sum_{j=1}^{n}\left[w_{2j-1}\cos(j\omega_{\mathrm{ex}}t) + w_{2j}\sin(j\omega_{\mathrm{ex}}t)\right], \tag{18b}$$

$$u = v_0 + \sum_{j=1}^{n}\left[v_{2j-1}\cos(j\omega_{\mathrm{ex}}t) + v_{2j}\sin(j\omega_{\mathrm{ex}}t)\right] \tag{18c}$$

with the Fourier coefficients $\boldsymbol{q}_j(t) \in \mathbb{R}^4$, $v_j(t) \in \mathbb{R}$ and $w_j(t) \in \mathbb{R}$, the sampling frequency $\omega_{\mathrm{ex}} > 0$, the delay $\tilde{\tau} \in \{0, \tau\}$, and the order of the envelope model $n \in \mathbb{N}$ for all $j = 0, 1, \ldots, 2n$. Taking the derivative of (18b) with respect to time for $\tilde{\tau} = 0$, inserting the result and (18c) into (1) and comparing the sine-

and cosine-terms, yields

$$\frac{\mathrm{d}\boldsymbol{q}}{\mathrm{d}t} = A_q\boldsymbol{q} + B_q\boldsymbol{w} + \boldsymbol{f}_q(\boldsymbol{q}, \boldsymbol{q}_\tau, \boldsymbol{v}) \tag{19}$$

with the state vector $\boldsymbol{q} = [\boldsymbol{q}_0^{\mathrm{T}}, \boldsymbol{q}_1^{\mathrm{T}}, \ldots, \boldsymbol{q}_{2n}^{\mathrm{T}}]^{\mathrm{T}} \in \mathbb{R}^{8n+4}$, the input vectors $\boldsymbol{w} = [w_0, w_1, \ldots, w_{2n}]^{\mathrm{T}} \in \mathbb{R}^{2n+1}$ and $\boldsymbol{v} = [v_0, v_1, \ldots, v_{2n}]^{\mathrm{T}} \in \mathbb{R}^{2n+1}$, and the nonlinearity $\boldsymbol{f}_q(\boldsymbol{q}, \boldsymbol{q}_\tau, \boldsymbol{v}) \in \mathbb{R}^{8n+4}$. Herein, the system matrix and the input matrix are given by

$$A_q = \begin{bmatrix} A & 0 & 0 & \cdots & 0 & 0 \\ 0 & A & -\omega_{\mathrm{ex}} I_4 & \cdots & 0 & 0 \\ 0 & \omega_{\mathrm{ex}} I_4 & A & \cdots & 0 & 0 \\ \vdots & \vdots & \vdots & \ddots & \vdots & \vdots \\ 0 & 0 & 0 & \cdots & A & -n\omega_{\mathrm{ex}} I_4 \\ 0 & 0 & 0 & \cdots & n\omega_{\mathrm{ex}} I_4 & A \end{bmatrix},$$

$$B_q = \begin{bmatrix} \boldsymbol{b} & 0 & 0 & \cdots & 0 & 0 \\ 0 & \boldsymbol{b} & 0 & \cdots & 0 & 0 \\ 0 & 0 & \boldsymbol{b} & \cdots & 0 & 0 \\ \vdots & \vdots & \vdots & \ddots & \vdots & \vdots \\ 0 & 0 & 0 & \cdots & \boldsymbol{b} & 0 \\ 0 & 0 & 0 & \cdots & 0 & \boldsymbol{b} \end{bmatrix}$$

with the matrix $A = A_0|_{u_{\mathrm{DC}}=0}$ with A_0 from (3a), the vector $\boldsymbol{b} = [0, 1/(\rho h), 0, 0]^{\mathrm{T}} \in \mathbb{R}^4$, and the identity matrix $I_4 \in \mathbb{R}^{4\times4}$. The dimensions of the matrices are given by $A_q \in \mathbb{R}^{(8n+4)\times(8n+4)}$ and $B_q \in \mathbb{R}^{(8n+4)\times(2n+1)}$. In addition, the nonlinearity $\boldsymbol{f}_q(\boldsymbol{q}, \boldsymbol{q}_\tau, \boldsymbol{v}_2)$ represents the coupling between the modes and it can be derived by truncating higher modes. The amplitude of the envelope is given by

$$r_i = q_{i,0} + \sum_{j=1}^{n} \sqrt{q_{i,2j-1}^2 + q_{i,2j}^2}$$

for all $i = 1, 2, 3, 4$ [16].

IV. NUMERICAL RESULTS

Subsequently, the results of the bifurcation analysis in Section III are validated numerically. To this end, the numerical parameters from Table 1 are used. In particular, the critical points with theses parameters in the delay-free case are given by $k_{\mathrm{H}}^{+} = 0.4067$ and $k_{\mathrm{H}}^{-} = -1.9990$. The analysis is done as follows: First, the locations of (11) are analyzed, so that different regimes with different number of critical points can be identified. Second, the conditions for the emergence of the Andronov-Hopf bifurcations of system (1) are analyzed numerically in terms of the feedback strengths k_1 and k_2. Third, the steepest change of the characteristic frequency ω_{H} is analyzed and finally the reaction of (1) at the critical point τ_{H} is evaluated.

Following [47], the locations of the zeros z_0 of (11) are characterized by computing the discriminant of (11) and its corresponding auxiliary variables. The results are visualized in Figure 3. Here, the discriminant is shown in Figure 3(a), while the real zeros and positive zeros are localized in Figures 3(b) and 3(c). In particular, the positive zeros are

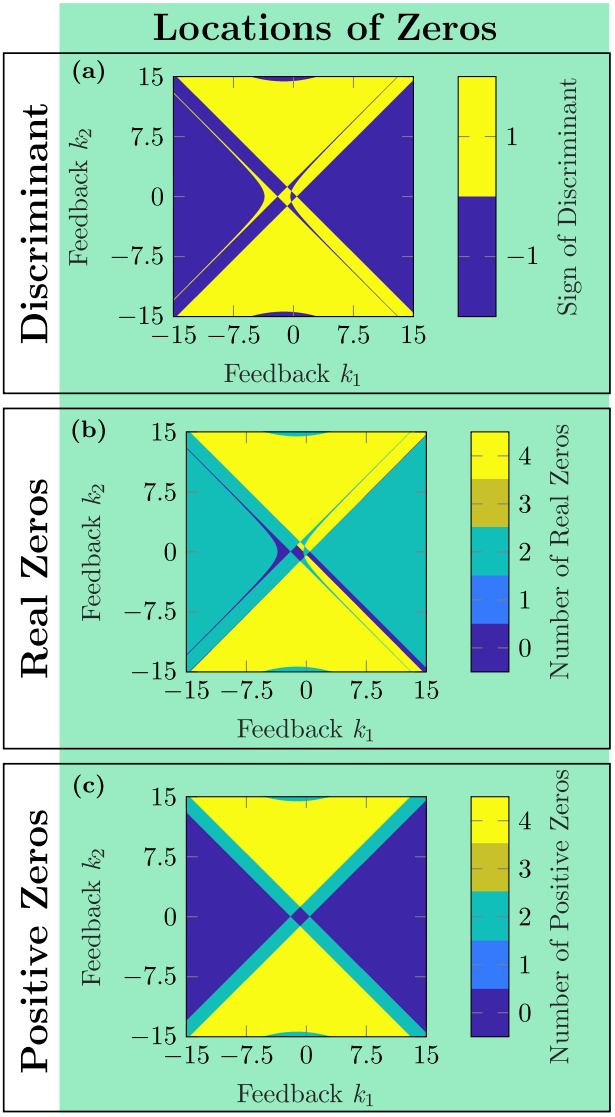

FIGURE 3. Color map of the discriminant, the number of real zeros, and the number of positive zeros of polynomial (13).

determined by computing the real-valued zeros and asserting condition (12). As expected, the number of possible zeros of (13) varies between 0 and 4. However, the regions for these solutions have a rather complex shape and additional constraints have to be applied. First of all, the characteristic frequency ω_{H} is computed by taking the square root of zeros of (13), so that these zeros have to be positive. In addition, (12) has to be satisfied, since (11) and (10) are otherwise not equivalent.

After applying these constraints and solving (11) numerically, the critical delay $\tau_{\mathrm{H},i}$ and the characteristic frequency at the critical point $\omega_{\mathrm{H},i}$ for all $i = 1, 2, 3, 4$ are obtained. In particular, the critical delays are computed by

$$\tau_{\mathrm{H},m}[l] = \frac{\arcsin\left(\frac{\omega_{\mathrm{H},m}^4 - a_2\omega_{\mathrm{H},m}^2 + a_0}{k_2 b_1 \omega_{\mathrm{H},m}}\right) + 2\pi l}{\omega_{\mathrm{H},m}} \tag{20}$$

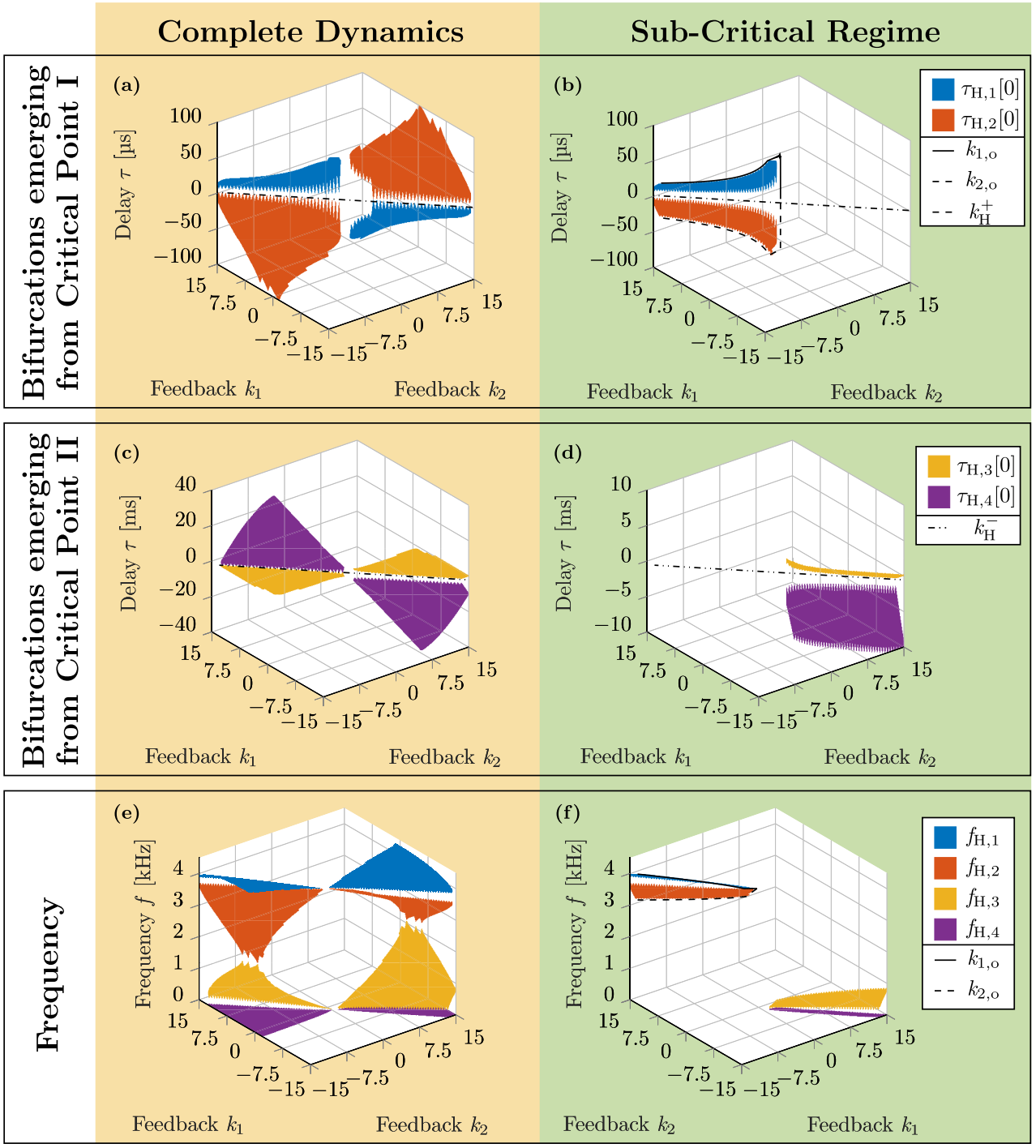

FIGURE 4. Critical delays $\tau_{H,m}[0]$, critical feedback strengths $k_H^{\pm}$, and characteristic frequencies $f_{H,m}$ at the critical point for all $m = 1, 2, 3, 4$ as a function of the feedback strengths k_1 and k_2. Here, the critical delays $\tau_{H,m}[0]$ for all $m = 1, 2, 3, 4$ are separated based on their emergence from the critical points $k_H^{\pm}$ of the MEMS sensor with undelayed feedback. Note that the characteristic frequency is given by as the normalized frequency, i.e., $f_H = \omega_H/(2\pi)$. In addition, the critical delay and characteristic frequency in terms of the steepest change k_o are visualized by the solid and dashed line. (a), (c), (e) The complete dynamics of system (1). (b), (d), (f) The sub-critical regime of (1).

for the solution indices $l \in \mathbb{Z}$ and $m = 1, 2, 3, 4$, so that there infinitely many solutions. Here, the solution index is assumed to be given by $l = 0$. The results are visualized in Figure 4. The dynamic regimes are divided into the complete dynamics and the sub-critical regime, which is determined by the condition $|k_1 + k_2| \leq |k_H^{\pm}|$ with the critical feedback strength $k_H^{\pm}$. The complete dynamics is depicted in Figures 4(a), 4(c), and 4(e), while the sub-critical regime

is shown in Figures 4(b), 4(d), and 4(f). This separation has been done since both regimes can be interesting for different applications. For instance, the MEMS sensor has to be driven to the sub-critical regime, if it is used as an acoustic sensor. Otherwise, the emerging limit cycle,[1] will distort the external stimuli.

It can be observed in Figures 4(a)-(d) that the solutions of the critical delay $\tau_{\mathrm{H},i}$ for all $i = 1, 2, 3, 4$ are closely related to the critical feedback strengths $k_{\mathrm{H}}^{\pm}$, since the critical delays $\tau_{\mathrm{H},1}$ and $\tau_{\mathrm{H},2}$ or $\tau_{\mathrm{H},3}$ and $\tau_{\mathrm{H},4}$ vanish by choosing $k_1 + k_2 = k_{\mathrm{H}}^{+}$ or $k_1 + k_2 = k_{\mathrm{H}}^{-}$. Moreover, it follows from Figures 4(e) and 4(f) that the characteristic frequency can be either increased or decreased by assigning the delay τ and the feedback strengths k_1 and k_2 accordingly. Hence, by exploiting the controllable delay, the characteristic frequency can move below the lower limit of the characteristic frequency, which is determined by the geometry and material of the MEMS sensor. These frequencies can be reached even though the critical delays $\tau_{\mathrm{H},2}$ and $\tau_{\mathrm{H},4}$ are negative since (20) has infinitely many solutions for $\tau_{\mathrm{H},m}$ for all $m = 1, 2, 3, 4$.

In addition, note that the solid black lines and dashed black lines in Figures 4(b) and 4(f) depict the time delay $\tau_{\mathrm{H},1}$ and $\tau_{\mathrm{H},2}$ and characteristic frequency $f_{\mathrm{H},1}$ $f_{\mathrm{H},2}$ in the sub-critical regime in terms of the steepest change $\boldsymbol{k}_{\mathrm{o}}$. These have been computed for the weight $\epsilon = 3.45 \times 10^{-3}$ and the initial conditions $k_{1,0} = 1.001 \times k_{\mathrm{H}}^{+}$ and $k_{1,0} = -0.001 \times k_{\mathrm{H}}^{+}$. It turns out that the steepest change of the feedback strengths k_1 and k_2 in the sub-critical regime can be split into two regimes. On the one hand, the steepest change follows the conditions (12). On the other hand, the feedback strengths are constrained by $|k_1 + k_2| < |k_{\mathrm{H}}^{\pm}|$. Finally, the crossing condition is evaluated by determining the sign of the sensitivity d for the four possible critical points in terms of the feedback strengths k_1 and k_2. The results are visualized in Figure 5. Here, the sensitivity of the critical delay $\tau_{\mathrm{H},1}$ and $\tau_{\mathrm{H},2}$ are shown in Figure 5(a) and the sensitivity of the critical delay $\tau_{\mathrm{H},2}$ and $\tau_{\mathrm{H},3}$ are shown in Figure 5(b). The sign for each sensitivity stays constant for all feedback strengths k_1 and k_2. Thus, a pair of complex conjugated eigenvalues will cross from the complex left half-plane to the right half-plane, if the critical delays $\tau_{\mathrm{H},1}$ and τ_{H_3} are surpassed. In contrast, a pair of complex conjugated eigenvalues will cross from the complex right half-plane to the left half-plane, if the critical delays $\tau_{\mathrm{H},2}$ and τ_{H_4} are surpassed. This implies that the characteristic frequency can be decreased, if

$$(\tau > \tau_{\mathrm{H},2}[l] \wedge \tau_{\mathrm{H},2}[l] < \tau_{\mathrm{H},2}[l]) \vee (\tau > \tau_{\mathrm{H},4}[l] \wedge \tau_{\mathrm{H},4}[l] < \tau_{\mathrm{H},3}[l]).$$

for the solution indices $l \in \mathbb{Z}$. To simplify the bifurcation analysis, the frequency tunability of the characteristic frequencies $\omega_{\mathrm{H},1}$ and $\omega_{\mathrm{H},2}$ and positive critical delays $\tau_{\mathrm{H},1}$ and $\tau_{\mathrm{H},2}$ as a function of k_1 for the steepest change are depicted in Figures 6(a) and 6(b). As mentioned, the characteristic frequency of the system (1) can be both increased and decreased. However, its characteristic frequency has a lower limit in the sub-critical regime, since a Hopf-Hopf bifurcation[2] emerges at the critical delay $\tau_{\mathrm{HH}} = 272\ \mu\mathrm{s}$ and the critical feedback strength $k_{1,\mathrm{HH}} = 10.37$, so that the characteristic frequency in the sub-threshold regime can be decreased down to 400 Hz while following the steepest change.

Moreover, the eigenvalue, which is closest to the imaginary axis has been computed. In particular, the characteristic frequency is determined by the imaginary part of this eigenvalue. This is shown in Figure 6(c). The characteristic frequency can also be tuned by the feedback k_1 and k_2, if the bifurcation parameter is not at the critical point. In addition, the real part is visualized in Figure 6(d). This can be used to tune the gain of the MEMS sensor, so that it follows that

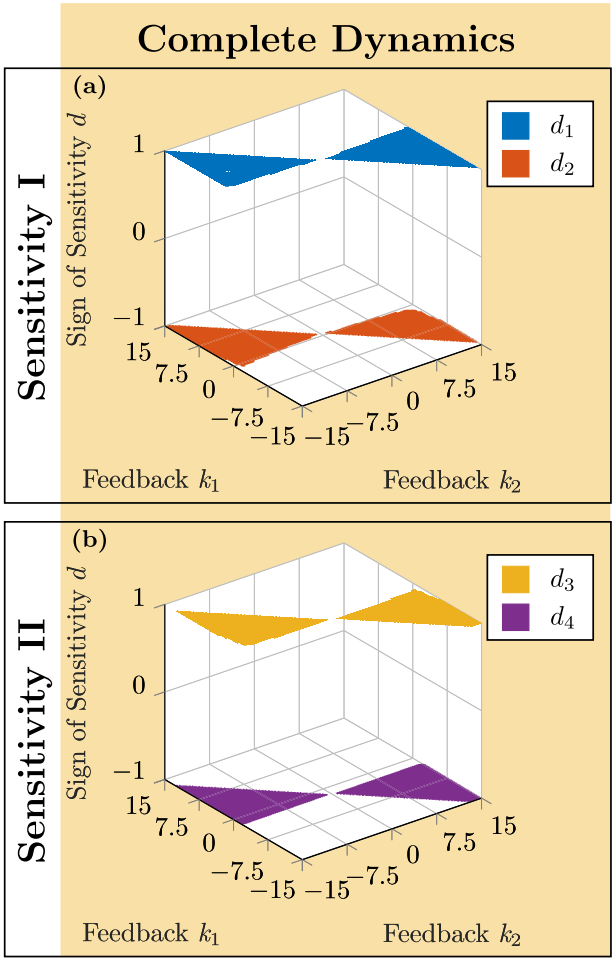

FIGURE 5. Sign of the sensitivities d_1, d_2, d_3, and d_4 at their respective critical points.

[1] It has to be stressed that this limit cycle can be only observed in experiments, see, e.g. [15], since the physical system is passive. In comparison, the mathematical model of this system does not capture this because the cantilever is assumed to satisfy the Bernoulli assumption.

[2] A Hopf-Hopf bifurcation emerges, if two complex-conjugated pairs of eigenvalues are on the imaginary axis [26]. For this, two bifurcation parameters are needed.

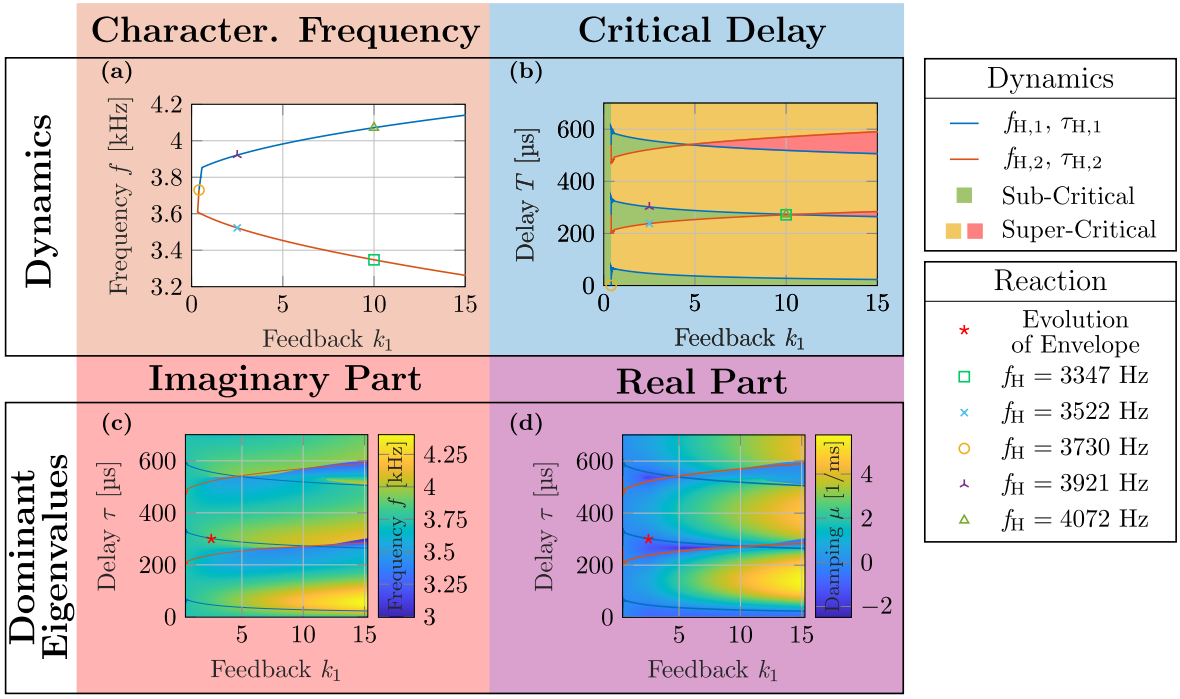

FIGURE 6. Dynamics of system (1) for the steepest change of the characteristic frequency. Note that the characteristic frequency is given by as the normalized frequency, i.e., $f_H = \omega_H/(2\pi)$. (a), (b) 2 dimensional representation of the necessary condition of the Hopf Theorem. The feedback strengths k_1 and k_2 follow the steepest change of the characteristic frequency $f_{H,1}$ and $f_{H,2}$ (c), (d) Eigen value, which are closest to the imaginary axis. In particular, the imaginary part of this eigenvalues can be used to predict the characteristic frequency. While the real part of this eigen value determines the gain and the Q-factor of the MEMS sensor.

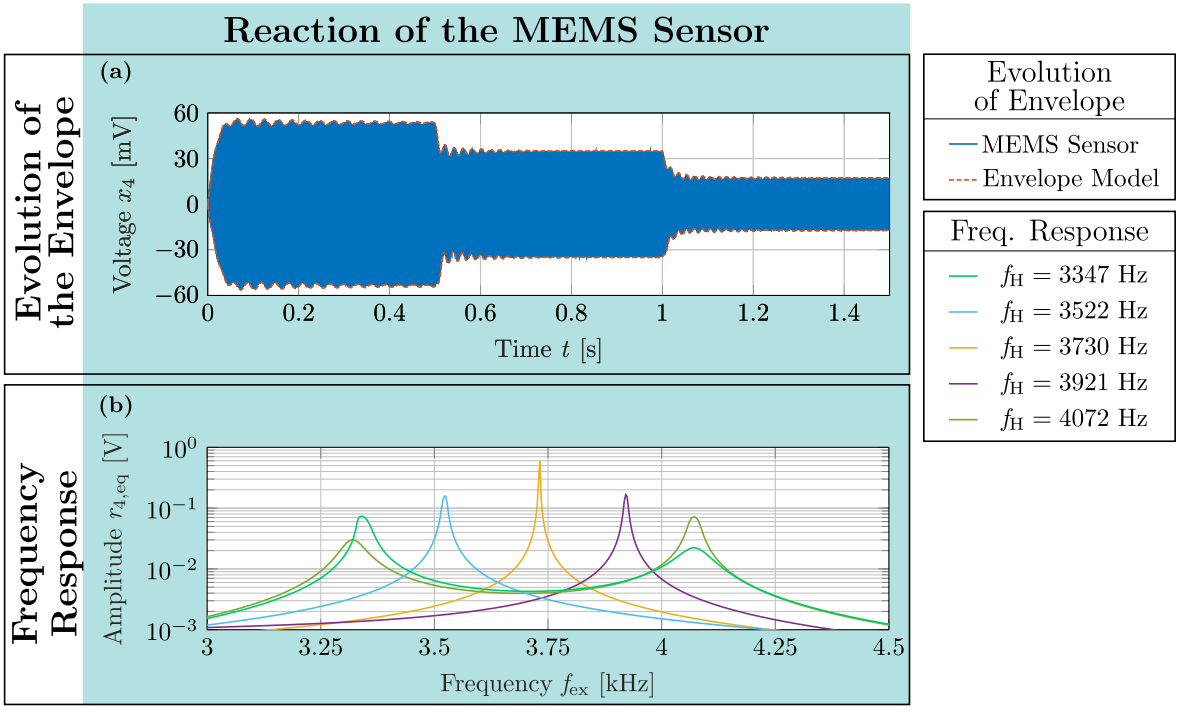

FIGURE 7. Reaction of the MEMS sensor with a delayed feedback. (a) Comparison between the evolution of the amplitude r_4 of the envelope model (19) and the voltage x_4 of the dominant system (1). (b) Amplitude $r_{4,eq}$ of envelope model as a function of the excitation frequency $f_{ex} = \omega_{ex}/(2\pi)$ of an harmonic stimuli. The parameters for the different responses are given by the markers in Figure 6.

gain and frequency can be tuned by assigning the controllable parameters accordingly.

Finally, the envelope of the harmonically excited MEMS sensor is evaluated in Figure 7. On the one hand, the evolution

TABLE 1. Parameters of the MEMS sensor.

Parameter		Value
Frequency	ω_0	$2\pi \times 3.73\,\text{kHz}$
Q-Factor	Q_0	92
Offset voltage	u_{DC}	$-0.3\,\text{V}$
Product of transfer factors	$\alpha \cdot \gamma$	$329,156,873.4\,\frac{\text{m}^2}{\text{A}^2\text{s}^3}$
Transfer factor	α	$19.2\,\frac{\text{m}^2}{\text{Ks}^2}$
	γ	$1.7144 \times 10^7\,\frac{\text{K}}{\text{A}^2\text{s}}$
	ζ	$1.0972 \times 10^5\,\frac{\text{K}}{\text{V}^2\text{s}}$
Time constant	β	$256.4\,\frac{1}{\text{s}}$
	T	$10^{-3}\,\frac{1}{\text{s}}$
Resistance of the heater	R	$12.5\,\Omega$
Calibration factor	κ	$273 \times 10^3\,\frac{\text{V}}{\text{m}}$
Height	h	$1.45 \times 10^{-6}\,\text{m}$
Density of silicon	ρ_{Si}	$2,329\,\frac{\text{kg}}{\text{m}^3}$

of the envelope model for $n = 2$ and the evolution of the MEMS sensor is compared in Figure 7(a). For this, the parameters k_1, k_2, τ, and ω_{ex} follow from the steepest change of the characteristic frequency, as they are depicted in Figures 6(c) and 6(d). In addition, the external excitation is given by

$$f_{\text{ex},1} = \begin{cases} \hat{f}_{\text{ex},1}, & \text{if } t < t_1, \\ \hat{f}_{\text{ex},2}, & \text{if } t \in [t_1, t_2), \\ \hat{f}_{\text{ex},3}, & \text{if } t \in [t_2, t_3), \end{cases} \qquad f_{\text{ex},j} = 0\,\text{Pa},$$

with the amplitudes $\hat{f}_{\text{ex},1} = 15 \times 10^{-4}\,\text{Pa}$, $\hat{f}_{\text{ex},2} = 10 \times 10^{-4}\,\text{Pa}$, and $\hat{f}_{\text{ex},3} = 5 \times 10^{-4}\,\text{Pa}$ and the time instances $t_k = 500k$ ms for all $j \neq 1$ and $k \in \{1, 2, 3\}$. It turns out that it is sufficient to approximate the envelope of the MEMS sensor with $n = 2$, since the MEMS sensor acts like a band pass filter, so that higher oscillation are suppressed. On the other hand, the frequency tunability of the MEMS sensor is evaluated by visualizing the frequency response of the amplitude $r_{4,\text{eq}}$ for different parameter configurations. This is depicted in Figures 7(b). Herein, the parameters k_1, k_2, and τ follow from the steepest change, as they are depicted in Figure 6(a) and 6(b). The external excitation is given by

$$f_{\text{ex},1} = 2 \times 10^{-3}\,\text{Pa}, \quad f_{\text{ex},j} = 0\,\text{Pa},$$

for all $j \neq 1$. The results of the bifurcation analysis indeed suggest that the characteristic frequency of the system (1) can be tuned flexibly by a delayed feedback loop and an undelayed feedback loop. In addition, local maxima for the amplitudes $r_{4,\text{eq}}$ with a feedback strength k_1 can observed. This comes from the fact that (1) is close to the Hopf-Hopf bifurcation, such that the effects of the Hopf-Hopf bifurcation become visible.

V. CONCLUSION

A new control approach has been proposed to tune the characteristic frequency of a cantilevered MEMS sensor. The designed control strategy relies on two active feedback loops, with and without time delay, whose interplay leads to the emergence of an Andronov-Hopf bifurcations in the system. With this, the characteristic frequency of the cantilevered MEMS sensor can be flexibly tuned by assigning the feedback strengths and delay accordingly. Remarkably, along with the increase of the characteristic frequency, the proposed approach allows to decrease the frequency down to 90% of its original value. The latter is known to be a challenging task in the MEMS sensors community, previously achievable only by severely constrained and resource consuming methods [3], [4].

Finally, as the considered setup is realized on a field programmable gate array, the controllable delayed feedback can be implemented by saving the output and retrieving the data after the desired delay is reached. Hence, due to a relatively short time delay within a range of hundreds of microseconds, the proposed control approach has a great promise for the hardware implementation and particularly feasible for neuromorphic acoustic sensing applications.

APPENDIX
PARAMETERS OF THE MEMS SENSOR

The numerical parameters of the MEMS sensor are given in Table 1. These parameters were determined in experiments and thus describe an actual MEMS sensor.

COMPETING INTERESTS

The authors declare no competing interests.

CODE AVAILABILITY

The custom-developed codes for the MATLAB simulation are available from the corresponding author upon request.

REFERENCES

[1] K. Tanaka, Y. Mochida, M. Sugimoto, K. Moriya, T. Hasegawa, K. Atsuchi, and K. Ohwada, "A micromachined vibrating gyroscope," *Sens. Actuators A, Phys.*, vol. 50, nos. 1–2, pp. 111–115, Aug. 1995.

[2] M. Chiao and L. Lin, "Post-packaging tuning of microresonators by pulsed laser deposition," in *TRANSDUCERS 12th Int. Conf. Solid-State Sensors, Actuat. Microsystems. Dig. Tech. Papers*, vol. 2, Boston, MA, USA, Jun. 2003, pp. 1820–1823.

[3] R. R. A. Syms, "Electrothermal frequency tuning of folded and coupled vibrating micromechanical resonators," *J. Microelectromech. Syst.*, vol. 7, no. 2, pp. 164–171, Jun. 1998.

[4] Y.-C. Lee, L.-K. Wang, Y.-C. Chuang, H.-C. Hong, and Y. Chiu, "Electrothermal tunable MEMS oscillators for MEMS-based reservoir computing," *IEEE Sensors Lett.*, vol. 8, no. 7, pp. 1–4, Jul. 2024.

[5] H. F. J. Rolf and T. Meurer, "Enabling tunability of a MEMS sensor with a geometric nonlinearity1," *IFAC-PapersOnLine*, vol. 58, no. 5, pp. 66–71, 2024.

[6] J. J. Yao and N. C. MacDonald, "A micromachined, single-crystal silicon, tunable resonator," *J. Micromech. Microeng.*, vol. 5, no. 3, pp. 257–264, Sep. 1995.

[7] K. B. Lee and Y.-H. Cho, "A triangular electrostatic comb array for micromechanical resonant frequency tuning," *Sens. Actuators A, Phys.*, vol. 70, nos. 1–2, pp. 112–117, Oct. 1998.

[8] S. G. Adams, F. M. Bertsch, and N. C. MacDonald, "Independent tuning of the linear and nonlinear stiffness coefficients of a micromechanical device," in *Proc. 9th Int. Workshop Micro Electromechanical Syst.*, Feb. 2002, pp. 32–37.
[9] H. Ding, L. Fu, Y. Wang, and J. Xie, "Resonant frequency tunable silicon fishbone-shaped MEMS double ended tuning fork," in *Proc. IEEE 11th Annu. Int. Conf. Nano/Micro Engineered Mol. Syst. (NEMS)*, Apr. 2016, pp. 233–236.
[10] K. Bang Lee, L. Lin, and Y.-H. Cho, "A frequency-tunable microactuator with a varied comb-width profile," in *Proc. 17th IEEE Int. Conf. Micro Electro Mech. Systems. Maastricht MEMS Tech. Dig.*, Jan. 2004, pp. 257–260.
[11] T. Ivanov, "Piezoresistive cantilevers with an integrated bimorph actuator," Ph.D. dissertation, Dept. Phys., Kassel Univ., Kassel, Germany, 2004.
[12] D. Roeser, S. Gutschmidt, T. Sattel, and I. W. Rangelow, "Tip motion—Sensor signal relation for a composite SPM/SPL cantilever," *J. Microelectromech. Syst.*, vol. 25, no. 1, pp. 78–90, Feb. 2016.
[13] C. Lenk, A. Ekinci, I. W. Rangelow, and S. Gutschmidt, "Active, artificial hair cells for biomimetic sound detection based on active cantilever technology," in *Proc. 40th Annu. Int. Conf. IEEE Eng. Med. Biol. Soc. (EMBC)*, Jul. 2018, pp. 4488–4491.
[14] C. Lenk, L. Seeber, M. Ziegler, P. Hövel, and S. Gutschmidt, "Enabling adaptive and enhanced acoustic sensing using nonlinear dynamics," in *Proc. IEEE Int. Symp. Circuits Syst. (ISCAS)*, Oct. 2020, pp. 1–4.
[15] C. Lenk, P. Hövel, K. Ved, S. Durstewitz, T. Meurer, T. Fritsch, A. Männchen, J. Küller, D. Beer, T. Ivanov, and M. Ziegler, "Neuromorphic acoustic sensing using an adaptive microelectromechanical cochlea with integrated feedback," *Nature Electron.*, vol. 6, no. 5, pp. 370–380, May 2023.
[16] H. F. Johann Rolf and T. Meurer, "Amplitude control for an artificial hair cell undergoing an andronov-hopf bifurcation," *IFAC-PapersOnLine*, vol. 56, no. 1, pp. 181–186, 2023.
[17] H. F. J. Rolf and T. Meurer, "On coupled oscillators modeling bio-inspired acoustic sensors: Bifurcation analysis toward tunability enhancement," *Chaos, Interdiscipl. J. Nonlinear Sci.*, vol. 34, no. 10, pp. 1–34, Oct. 2024.
[18] K. Ved, C. Lenk, T. Ivanov, P. Hövel, and M. Ziegler, "Bio-inspired, adaptive acoustic sensor: Sensing properties in dependence of feedback parameters," in *AIP Conf. Proc.*, vol. 3062, 2024, pp. 1–11.
[19] T. A. J. Duke and F. Jülicher, "Critical oscillators as active elements in hearing," in *Active Processes and Otoacoustic Emissions in Hearing*. Cham, Switzerland: Springer, 2008, pp. 63–92.
[20] A. J. Hudspeth, F. Jülicher, and P. Martin, "A critique of the critical cochlea: Hopf—A bifurcation—Is better than none," *J. Neurophysiology*, vol. 104, no. 3, pp. 1219–1229, Sep. 2010.
[21] M. Ospeck, V. M. Eguíluz, and M. O. Magnasco, "Evidence of a Hopf bifurcation in frog hair cells," *Biophysical J.*, vol. 80, no. 6, pp. 2597–2607, Jun. 2001.
[22] A. Kern and R. Stoop, "Essential role of couplings between hearing nonlinearities," *Phys. Rev. Lett.*, vol. 91, no. 12, Sep. 2003, Art. no. 128101.
[23] V. M. Eguíluz, M. Ospeck, Y. Choe, A. J. Hudspeth, and M. O. Magnasco, "Essential nonlinearities in hearing," *Phys. Rev. Lett.*, vol. 84, no. 22, pp. 5232–5235, May 2000.
[24] T. Gold, R. J. Pumphrey, and J. Gray, "Hearing. I. the cochlea as a frequency analyzer," *Proc. Roy. Soc. B, Biol. Sci.*, vol. 135, no. 881, pp. 462–491, Dec. 1948.
[25] T. Gold and J. Gray, "Hearing. II. the physical basis of the action of the cochlea," *Proc. Roy. Soc. B, Biol. Sci.*, vol. 135, no. 881, pp. 492–498, Dec. 1948.
[26] J. Guckenheimer and P. Holmes, *Nonlinear Oscillations, Dynamical Systems, and Bifurcations of Vector Fields*, vol. 42. Cham, Switzerland: Springer, 2013.
[27] J. E. Marsden and M. McCracken, *The Hopf Bifurcation and Its Applications* (Applied mathematical sciences). New York, NY, USA: Springer, 1976.
[28] G. F. Fussmann, S. P. Ellner, K. W. Shertzer, and N. G. Hairston Jr., "Crossing the Hopf bifurcation in a live predator-prey system," *Science*, vol. 290, no. 5495, pp. 1358–1360, Nov. 2000.
[29] J. Guckenheimer, R. M. Harris-Warrick, J. H. Peck, and A. R. Willms, "Bifurcation, bursting, and spike frequency adaptation," *J. Comput. Neurosci.*, vol. 4, no. 3, pp. 257–277, Jan. 1997.
[30] J. Guckenheimer and I. Labouriau, "Bifurcation of the Hodgkin and Huxley equations: A new twist," *Bull. Math. Biol.*, vol. 55, no. 5, pp. 937–952, Sep. 1993.
[31] E. M. Izhikevich, "Simple model of spiking neurons," *IEEE Trans. Neural Netw.*, vol. 14, no. 6, pp. 1569–1572, Nov. 2003.
[32] G.-B. Stan and R. Sepulchre, "Analysis of interconnected oscillators by dissipativity theory," *IEEE Trans. Autom. Control*, vol. 52, no. 2, pp. 256–270, Feb. 2007.
[33] D. G. Aronson, G. B. Ermentrout, and N. Kopell, "Amplitude response of coupled oscillators," *Phys. D, Nonlinear Phenomena*, vol. 41, no. 3, pp. 403–449, Apr. 1990.
[34] F. Gomez, T. Lorimer, and R. Stoop, "Signal-coupled subthreshold hopf-type systems show a sharpened collective response," *Phys. Rev. Lett.*, vol. 116, no. 10, Mar. 2016, Art. no. 108101.
[35] R. Van Buskirk and C. Jeffries, "Observation of chaotic dynamics of coupled nonlinear oscillators," *Phys. Rev. A, Gen. Phys.*, vol. 31, no. 5, pp. 3332–3357, May 1985.
[36] D. Premraj, K. Manoj, S. A. Pawar, and R. I. Sujith, "Effect of amplitude and frequency of limit cycle oscillators on their coupled and forced dynamics," *Nonlinear Dyn.*, vol. 103, no. 2, pp. 1439–1452, Jan. 2021.
[37] D. V. Ramana Reddy, A. Sen, and G. L. Johnston, "Time delay effects on coupled limit cycle oscillators at Hopf bifurcation," *Phys. D, Nonlinear Phenomena*, vol. 129, nos. 1–2, pp. 15–34, May 1999.
[38] J. Wei and C. Zhang, "Stability analysis in a first-order complex differential equations with delay," *Nonlinear Anal., Theory, Methods Appl.*, vol. 59, no. 5, pp. 657–671, Nov. 2004.
[39] H. F. J. Rolf, R. Kumar, and T. Meurer, "Effects of time delay on the resonance frequency of andronov-hopf bifurcations in neuromorphic devices," *IFAC-PapersOnLine*, vol. 58, no. 17, pp. 13–18, 2024.
[40] W. Michiels and S.-I. Niculescu, *Stability and Stabilization of Time-Delay Systems*. Philadelphia, PA, USA: Society for Industrial and Applied Mathematics, 2007.
[41] H. Smith, *An Introduction To Delay Differential Equations With Applications* (Texts in Applied Mathematics), vol. 57. New York, NY, USA: Springer, 2011.
[42] J.-P. Richard, "Some trends and tools for the study of time-delay systems," in *Proc. 2nd Conf. IMACS-IEEE Conf. Comput. Eng. Syst. Appl.*, Apr. 1998, pp. 27–43.
[43] J. N. Reddy, *Energy Principles and Variational Methods in Applied Mechanics*. Hoboken, NJ, USA: Wiley, 2017.
[44] V. A. Caliskan, O. C. Verghese, and A. M. Stankovic, "Multifrequency averaging of DC/DC converters," *IEEE Trans. Power Electron.*, vol. 14, no. 1, pp. 124–133, Jan. 1999.
[45] M. Egretzberger and A. Kugi, "A dynamical envelope model for vibratory gyroscopes," *Microsyst. Technol.*, vol. 16, no. 5, pp. 777–786, May 2010.
[46] M. Egretzberger, F. Mair, and A. Kugi, "Model-based control concepts for vibratory MEMS gyroscopes," *Mechatronics*, vol. 22, no. 3, pp. 241–250, Apr. 2012.
[47] E. L. Rees, "Graphical discussion of the roots of a quartic equation," *Amer. Math. Monthly*, vol. 29, no. 2, pp. 51–55, Feb. 1922.

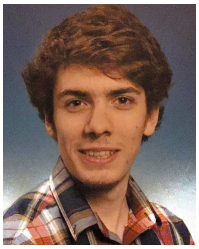

HERMANN FOLKE JOHANN ROLF received the M.Sc. degree in electrical engineering and information technology from Kiel University, Kiel, Germany, in 2021. He was a Research Associate with the Automation and Control Group, Faculty of Engineering, Kiel University, from 2021 to 2023. Since 2023, he has been a Research Associate at the Digital Process Engineering Group, Institute of Mechanical Engineering and Mechanics, Karlsruhe Institute of Technology (KIT), Karlsruhe, Germany. His research interests include control theory, neuromorphic engineering, and nonlinear dynamics.

PETRO FEKETA received the Ph.D. degree in mathematics from Taras Shevchenko National University of Kyiv, Ukraine.

He is currently a Lecturer in applied mathematics with Victoria University of Wellington, New Zealand. Before joining Victoria University of Wellington, he held postdoctoral positions at Kiel University, Germany; the Technical University of Kaiserslautern, Germany; and the University of Applied Sciences Erfurt, Germany. His research interests include the qualitative theory of smooth and discontinuous dynamical systems, stability and synchronization analysis of networked systems and interconnections of a large scale, the mathematical theory of multi-frequency oscillations, spiking neural networks, and neuromorphic computing. He is a member of New Zealand Mathematical Society (NZMS) and the Australia and New Zealand Industrial and Applied Mathematics (ANZIAM). He was a recipient of the KiNSIS Early Career Award, in 2021, and the Outstanding Reviewer Recognition Award from IEEE CONTROL SYSTEMS LETTERS, in 2022. He serves as a Reviewer Editor for *Frontiers in Control Engineering* (section ''Control Theory'').

THOMAS MEURER (Senior Member, IEEE) received the Diploma degree in process systems engineering from the University of Stuttgart, Stuttgart, Germany, in 2001, the M.Sc. degree in engineering science and mechanics from Georgia Institute of Technology, Atlanta, GA, USA, in 2000, and the Ph.D. (Dr.-Ing.) degree from the University of Stuttgart, in 2005.

From 2005 to 2007, he was a Postdoctoral Fellow with the Chair of System Theory and Automatic Control, Saarland University, Saarbrücken, Germany. In 2007, he joined the Automation and Control Institute, TU Vienna, Vienna, Austria, as a Senior Researcher, where he was appointed Associate Professor (Privatdozent), in 2012. From 2012 to 2023, he was a Full Professor and the Head of the Automatic Control Group, Kiel University, Kiel, Germany. Since 2023, he has been a Full Professor of digital process engineering and sustainable materials and energy and the Head of the Automatic Control Group, Institute of Mechanical Process Engineering and Mechanics, Karlsruhe Institute of Technology (KIT), Karlsruhe, Germany. His research interests include control of distributed parameter systems, nonlinear control theory, observer design, and optimal control with applications in robotics, production processes, mechatronics, marine systems, and process systems engineering. He received the VDI/GMA Eugen Hartmann Award, in 2009; the Cardinal Innitzer Award, in 2012; the IFAC Congress Best Interactive Paper Prize from the 2017 IFAC World Congress; and the Control Engineering Practice Paper Prize Award, in 2020. He was the Chair of the IFAC TC 2.6 on Distributed Parameter Systems, from 2011 to 2017, and the IEEE-CSS TC Distributed Parameter Systems, from 2019 to 2022. He is an Associate Editor of *Automatica*, *Mechatronics* (IFAC), IEEE TRANSACTIONS ON CONTROL SYSTEMS TECHNOLOGY, and *Mathematical Control and Related Fields*.